

A constrained reconstruction technique of hyperelasticity parameters for breast cancer assessment

Hatef Mehrabian¹, Gordon Campbell^{2,3,4} and Abbas Samani^{1,2}

¹ Department of Electrical & Computer Engineering, University of Western Ontario, London, ON, Canada

² Department of Medical Biophysics, University of Western Ontario, London, ON, Canada

³ Imaging Research Laboratories, Robarts Research Institute, London, ON, Canada

⁴ National Research Council, London, ON, Canada

E-mail: asamani@uwo.ca

Received 21 May 2010, in final form 6 September 2010

Published 19 November 2010

Online at stacks.iop.org/PMB/55/7489

Abstract

In breast elastography, breast tissue usually undergoes large compression resulting in significant geometric and structural changes. This implies that breast elastography is associated with tissue nonlinear behavior. In this study, an elastography technique is presented and an inverse problem formulation is proposed to reconstruct parameters characterizing tissue hyperelasticity. Such parameters can potentially be used for tumor classification. This technique can also have other important clinical applications such as measuring normal tissue hyperelastic parameters *in vivo*. Such parameters are essential in planning and conducting computer-aided interventional procedures. The proposed parameter reconstruction technique uses a constrained iterative inversion; it can be viewed as an inverse problem. To solve this problem, we used a nonlinear finite element model corresponding to its forward problem. In this research, we applied Veronda–Westmann, Yeoh and polynomial models to model tissue hyperelasticity. To validate the proposed technique, we conducted studies involving numerical and tissue-mimicking phantoms. The numerical phantom consisted of a hemisphere connected to a cylinder, while we constructed the tissue-mimicking phantom from polyvinyl alcohol with freeze-thaw cycles that exhibits nonlinear mechanical behavior. Both phantoms consisted of three types of soft tissues which mimic adipose, fibroglandular tissue and a tumor. The results of the simulations and experiments show feasibility of accurate reconstruction of tumor tissue hyperelastic parameters using the proposed method. In the numerical phantom, all hyperelastic parameters corresponding to the three models were reconstructed with less than 2% error. With the tissue-mimicking phantom, we were able to reconstruct the ratio of the hyperelastic parameters reasonably accurately. Compared to the uniaxial test results, the average error of the ratios of the parameters reconstructed for inclusion to the

middle and external layers were 13% and 9.6%, respectively. Given that the parameter ratios of the abnormal tissues to the normal ones range from three times to more than ten times, this accuracy is sufficient for tumor classification.

(Some figures in this article are in colour only in the electronic version)

1. Introduction

Breast cancer is one of the most common forms of cancer in women. Worldwide, breast cancer is the second most common cancer after lung cancer (10.4% of all cancer incidence, both sexes counted) (World Health Organization International Agency for Research on Cancer 2003), and the fifth most common cause of cancer death (World Health Organization 2006). While breast screening using x-ray mammography has proven to be effective in women after menopause, its value is limited with younger women who have dense breasts and thus a more effective diagnostic technique is necessary. To develop such diagnostic technique, researchers have attempted to utilize the fact that changes in soft tissue stiffness are associated with the presence of pathology. In the case of breast cancer, a tumor or a suspicious cancerous growth is normally stiffer than normal background tissue. This stiffness ranges from 3–6 times the stiffness of fibroglandular tissue for malignant tumors to 13 times in the case of high-grade invasive ductal carcinoma (Ophir *et al* 1991). Breast manual palpation is based on this correlation between stiffness and tissue abnormality; however, it is not sufficiently sensitive in the cases where the tumor is small or is located deep within the breast. In such cases, the tumor cannot be detected by palpation during early stages (Gao *et al* 1996). While imaging can provide quantitative information about the disease, conventional cross-sectional imaging methods do not provide tissue parameters associated directly with the findings of palpation (Skovoroda *et al* 1995). Elastography, a novel imaging technique, was developed in which tissue stiffness or strain images are used to detect or classify tumors (Skovoroda *et al* 1995, Samani and Plewes 2007, Devi *et al* 2006). The goal of elastography is mapping the elastic properties of tissue (Young's modulus or shear modulus) in an anatomically meaningful way to provide clinical information about tissue abnormality (Gao *et al* 1996). Given their high water content, most soft tissues are known to be near incompressible. This property is characterized by Poisson's ratio values ranging from 0.490 to 0.499 (Manduca *et al* 2001, Barbone and Oberai 2007). In classic elastography, the tissue is assumed to exhibit linear elasticity. Assuming tissue incompressibility implies that the tissue's Poisson's ratio is known, and the only parameter required to characterize the tissue elastic behavior is its Young's modulus. In quasi-static elastography, the tissue is mechanically stimulated by applying very low frequency (less than 10 Hz) external compression. Tissue deformation resulting from mechanical stimulation is required to determine and map soft tissue elastic properties. For this purpose, MRI or ultrasound displacement data acquisition techniques are usually used (Cespedes *et al* 1993, Konofagou and Ophir 1998, Chenevert *et al* 1998). Assuming that the tissue is linear elastic and isotropic, many researchers have developed elastic modulus reconstruction techniques ranging from strain imaging to ones based on full inversion of the elasticity governing equations (Kallel and Bertrand 1996, Skovoroda *et al* 1994, Emelianov *et al* 1995, Sumi *et al* 1995, Doyley *et al* 2000). In general, the problem of elastic modulus reconstruction is a highly ill-posed inverse problem, especially in 3D. To overcome this problem, Plewes *et al* (2000), Samani *et al* (2003), Mehrabian and Samani (2008), and Samani *et al* (2001) proposed a constrained elastography technique. This method assumes

uniform elasticity modulus distribution throughout each tissue volume. Unlike strain imaging methods of elastography, this technique takes into account the non-uniform stress distribution throughout tissue volumes. The novelty of this method lies in the use of anatomical constraints to impose a discrete elasticity modulus distribution for the reconstruction (Samani *et al* 2001).

In elastography procedures, the breast is precompressed prior to the application of quasi-static or harmonic mechanical stimulation. This is done to minimize undesirable boundary effects. The amount of compression is chosen arbitrarily by the clinician. Given tissue nonlinearity, the tissue stiffness will depend significantly on the amount of tissue precompression. Indeed this issue has led to the very wide range of elastic modulus values reported in the literature for breast normal and pathological tissues. Hall *et al* (2009) showed that for invasive ductal carcinoma (IDC) the strain contrast increases at larger deformation compared to smaller deformation; whereas they showed that the opposite happens for fibroadenoma. This is because with large deformations, the assumptions for linear elastography are violated and hyperelastic models are required to solve these problems. Varghese *et al* (2000) stated that in nonlinear elastography, with large tissue compressions the contrast in elastography images increases significantly due to tissue nonlinear stress—strain relationship.

Although assuming that the tissue exhibits linear elastic behavior (as used in classic elastography) is valid when small external compression is applied, most soft tissues, especially breast tissues, deform significantly during typical elastography mechanical stimulation (Sciarretta *et al* 2002). This tissue deformation often exceeds the amount of deformation allowed with linear elastic models. To address the issues of precompression dependence and low SNR in elastography while considering the issue of linear elasticity validity, large external compression can be applied in conjunction with finite elasticity modeling. In finite elasticity, the tissue is modeled as hyperelastic material to account for the tissue intrinsic and geometric nonlinearities. Another highly important motivation for developing an elastography system capable of imaging tissue hyperelastic parameters is based on the *ex vivo* breast tissue hyperelastic parameter data obtained by O'Hagan and Samani (2009). These data indicated that some hyperelastic parameters are capable of classifying breast cancer with high confidence. Skovoroda *et al* (1999) showed that despite requirements of higher order derivatives of displacements for nonlinear reconstruction, their image quality rival those based on a simpler linear model. Sinkus *et al* (2002) used MR elastography to show that various breast tissue pathologies exhibit different nonlinear characteristics. Therefore, nonlinear (hyperelastic) elastography has a potential to be a highly specific breast cancer diagnosis technique.

Oberai *et al* (2009) assessed the feasibility of using nonlinear elasticity imaging of breast tissue in discerning malignant tumors from benign ones. They demonstrated that the distribution of nonlinear elastic parameters represents the mechanical properties of the tissue more accurately compared to linear parameters. Hyperelastic parameters reconstructed using nonlinear elastography are the intrinsic properties of the tissue and are independent of the boundary conditions (Erkamp *et al* 2004).

In this investigation we have extended the technique proposed by Samani *et al* (2001) to reconstruct tissue hyperelastic parameters. Similar to Samani *et al* (2001), we assume that tissue lesion is already detected by a conventional imaging modality and the purpose is to classify the lesion. The parameter reconstruction is formulated as an inverse problem that is solved iteratively. Each iteration involves a nonlinear finite element analysis followed by a hyperelastic parameter updating. In the parameter updating step, a system of linear equations needs to be solved. Depending on the used hyperelastic model, this linear system of equations can be highly ill conditioned. In such a case, we developed a novel hybrid regularization

algorithm consisted of a sequence of three different regularization techniques. For validation, we present a computational phantom study followed by a tissue-mimicking phantom study. Both of the computational and experimental phantoms consist of three different tissue types to represent the three different cancerous breast tissues (adipose, fibroglandular and tumor tissues). In these examples, a number of hyperelastic models commonly used in tissue modeling were tested. Results obtained from this investigation demonstrate the feasibility of reconstructing the hyperelastic parameters reasonably accurately. In an *ex vivo* breast tissue study, O'Hagan and Samani (2009) compared the performance of several hyperelastic models in classifying different tissues and showed that the Yeoh hyperelastic model has a good potential to distinguish between different pathological tissues. In this investigation, three different strain energy functions were used to model the nonlinear (hyperelastic) behavior of the tissues and their reconstruction results were compared.

2. Theory

Finite deformation formulation is necessary where tissue geometry changes significantly during loading. Such a geometry change is associated with the so-called geometric nonlinearity where it is assumed to be significant if the strain exceeds 5%. Combined with tissue intrinsic nonlinearity, geometric nonlinearity can be modeled using hyperelastic modeling. The elastic behavior of the material can be described using a strain energy function $U = U(F)$, where F denotes the deformation gradient tensor. Using this energy function for an incompressible hyperelastic material, its stress–strain relationship is as follows (Holzapfel and Ogden 2003):

$$S = \frac{dU}{dF} - pF^{-1} \quad \text{and} \quad \det(F) = 1, \quad (1)$$

where S is the first nominal stress and p is the hydrostatic pressure. For an isotropic material the strain energy function U is a function of the principal invariants of the left and right Cauchy Green strain tensor I_1, I_2, J . Thus the stress tensor for an incompressible, isotropic hyperelastic material can be written as (Holzapfel and Ogden 2003, Holzapfel 2000):

$$\sigma = F \frac{dU}{dF} - pI. \quad (2)$$

$$\sigma = \frac{2}{J} \text{DEV} \left[\left(\frac{\partial U}{\partial \bar{I}_1} + \frac{\bar{I}_1 \partial U}{\partial \bar{I}_2} \right) \bar{B} - \frac{\partial U}{\partial \bar{I}_2} \bar{B} \cdot \bar{B} \right] - pI, \quad (3)$$

where DEV represents the deviatoric part of the stress tensor, p is the hydrostatic pressure, I is the identity matrix, and \bar{B} and \bar{I}_i are

$$\bar{B} = \bar{F} \cdot \bar{F}^T, \quad \bar{F} = J^{-1/3} F \quad \text{and} \quad \bar{I}_i = J^{-2/3} I_i, \quad (4)$$

where $J = \det(F)$. Strain energy functions are defined as the functions of strain invariants (I_1, I_2, I_3) and a number of parameters called the 'hyperelastic parameters'. Various energy functions are chosen for different classes of materials based on previous experience. In this study, three strain energy functions—commonly used to model soft tissues—are used. The first strain energy function used here is the polynomial model with $N = 2$. The second-order polynomial strain energy function is the most commonly used function in rubber modeling and was recently used for breast tissue modeling (Samani and Plewes 2004). An important advantage of using this model is that it uses five parameters to model the mechanical behavior of the tissue; hence, it is capable of modeling the tissue response with high accuracy. The second model is the Yeoh model that has been recently used in various biomedical applications.

This model is only dependent on the first strain invariant while it is capable of modeling soft tissues with accuracy close to that of the polynomial model (Zhang 2004). The third is the Veronda–Westmann (V-W) model. This model has an exponential form and provides a very close fit to typical soft tissue stress–strain curves. This model was first introduced to model skin tissue and was later used to model lung tissue. Recently, it was applied to breast tissue modeling where it led to good results (Oberai *et al* 2009). Equations (5)–(7) represent the polynomial, Yeoh and Veronda–Westmann models, respectively:

$$U = \sum_{i+j=1}^N C_{ij}(\bar{I}_1 - 3)^i(\bar{I}_2 - 3)^j + \sum_{i=1}^N \frac{1}{D_i}(J_{el} - 1)^{2i} \tag{5}$$

$$U = \sum_{i=1}^N C_{i0}(\bar{I}_1 - 3)^i + \sum_{i=1}^N \frac{1}{D_i}(J_{el} - 1)^{2i}, \quad N = 3 \tag{6}$$

$$U = C_1[e^{C_3(\bar{I}_1-3)} - 1] - C_2(\bar{I}_2 - 3) + g(J_{el}), \tag{7}$$

where the C_s denote the hyperelastic parameters, J_{el} is the elastic volume strain, D_i is a compressibility coefficient and $g(J_{el})$ is a function of tissue compressibility. For an incompressible tissue $J_{el} = 1$ and thus $g(J_{el}) = 0$. Therefore, the second term in equations (5) and (6) and the third term in equation (7) disappear. As indicated earlier, in this work a constrained nonlinear elasticity reconstruction technique was developed for breast cancer assessment. To constrain the reconstruction, the hyperelastic parameters of the soft tissue are assumed to be uniform throughout each tissue type. The Yeoh model unlike the other two is independent of the second strain invariant (I_2). In practice, there are some difficulties in using the strain energy functions which are functions of I_2 in addition to I_1 (Yamashita and Kawabata 1995, Kaliske and Rothert 1997). These difficulties are (1) The sensitivity of the strain energy function to variations of I_2 and consequently its dependence on I_2 terms is generally much smaller than the sensitivity to variations of I_1 ; (2) it is difficult to measure the influence of I_2 on the strain energy function. Hence, eliminating the I_2 -dependent terms of the strain energy function generally improves the ability of the model in predicting tissue behavior.

To validate hyperelastic parameters reconstructed in the tissue-mimicking study presented in this investigation, these parameters were measured independently. For this purpose, cylindrical samples of each tissue type were made for uniaxial testing. By considering the diagonal form of the deformation gradient tensor (F) for tissue uniaxial loading and assuming that the direction of the principal stretches is oriented with the coordinate basis vectors, the uniaxial nominal stress can be obtained from the following equation in which λ is the uniaxial stretch (Holzapfel 2000):

$$T_{11} = \sigma_{11}/\lambda = 2 \left(\lambda = \frac{1}{\lambda^2} \right) \left(\frac{\partial U}{\partial I_1} + \frac{1}{\lambda} \frac{\partial U}{\partial I_2} \right). \tag{8}$$

3. Methods and materials

3.1. Constrained hyperelastic parameter reconstruction

The proposed reconstruction technique follows the constrained technique introduced by Samani *et al* (2003, 2001) which assumes that the breast tissue can be segmented such that the normal and pathological tissues can be separated reasonably accurately. This assumption was shown to be valid when MRI is being used for imaging the breast tissue. This technique

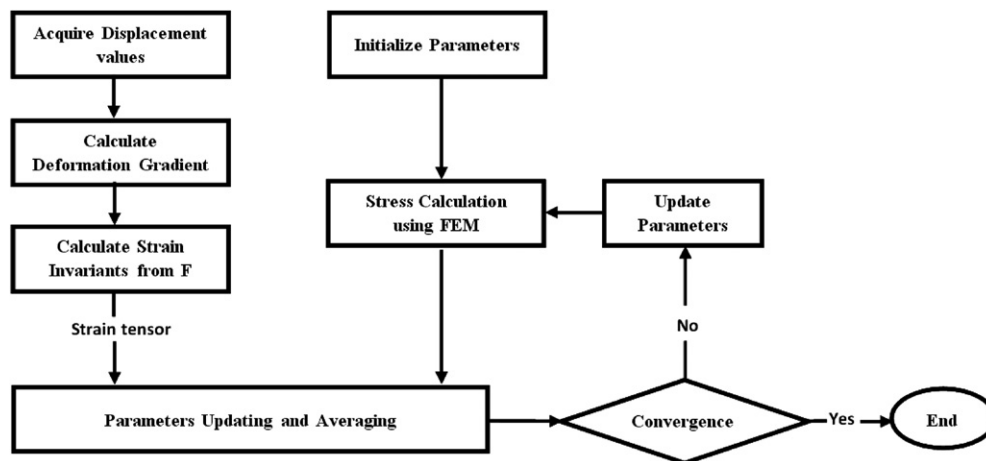


Figure 1. Flow chart illustrating the procedure of iterative reconstruction of hyperelastic parameters.

further assumes that inhomogeneity of each tissue is insignificant throughout its volume since *ex vivo* breast tissue data (Samani *et al* 2007) have shown that this inhomogeneity is little to modest. This implies that the hyperelastic parameters can be considered constant throughout the volume of each tissue.

To reconstruct the tissues' hyperelastic parameters, tissue displacements resulting from mechanical stimulation are acquired. In this investigation we acquire these displacements from two images corresponding to tissue pre-deformation and post-deformation. The developed algorithm of reconstructing tissue hyperelastic parameters is based on rearranging equation (3) into a linear system of equation (for polynomial and Yeoh models) or a nonlinear system of equations (for Veronda–Westmann model) in terms of the hyperelastic parameters. This led to an iterative algorithm, which involves parameter updating followed by nonlinear finite element analysis for stress calculation.

The iterative algorithm starts with an initial guess for the hyperelastic parameters of each tissue. These parameters are fed into a FE model of the tissue. This FE model uses a mesh that is generated from the segmented image of the tissue. The prescribed displacement boundary condition is applied to the top of the tissue, while the bottom side is fixed in the loading direction. The applied compression is simulated using ABAQUS V6.7 (Simulia, Dassault Systèmes) leading to tissue stress distribution. Hence, using the extracted displacement data in conjunction with the rearranged form of equation (3), the hyperelastic parameters were updated in each iteration until convergence was reached. The iterative parameter reconstruction process is summarized in the flowchart shown in figure 1 (Mehrabian and Samani 2008, 2009).

The step of parameter updating is carried out using the rearranged form of equation (3) in conjunction with the strain energy functions defined in equations (5) or (6). In the cases of the polynomial and Yeoh models, the rearranged form of equation (3) is the following linear system of equations:

$$\{\sigma\} = [A]\{C\}, \quad (9)$$

where $\{\sigma\}$ is the element stress tensor, $[A]$ is the coefficient matrix formed using nodal displacements and F tensor, and $\{C\}$ is the unknown hyperelastic parameter vector. This system was solved as described in the next section. For the Veronda–Westmann model case,

a different solution was developed because the rearranged form of equation (4) is a nonlinear function of the hyperelastic parameters, C , as given below:

$$\{\sigma\} = f(\{C\}), \quad (10)$$

where $f(\cdot)$ is a function of nodal displacements. This nonlinear system of equations was solved using a nonlinear least-squares method that involves iteratively using a combination of the preconditioned conjugate gradient optimization method, steepest descent method and Newton's optimization method. Using equations (9) or (10), the values of C_{ij} or C were calculated for each element in the FE mesh. In accordance with the constrained reconstruction approach, the parameters were then averaged over the entire volume of each tissue to obtain the updated parameters. The iterative algorithm is described in detail in the following pseudo-code.

- (1) Apply deformation to the tissue and measure its displacements.
- (2) Calculate the deformation gradient using the acquired displacements.
- (3) Calculate the strain invariants using the deformation gradients.
- (4) Form matrix $[A]$ in equation (9) or function $f(\cdot)$ in equation (10).
- (5) Generate FE mesh for the tissue using the segmented pre-deformation image of the tissue.
- (6) Generate a FE model of the tissue deformation using an ABAQUS FE solver and assign the loading specifications and boundary conditions.
- (7) Set the hyperelastic parameters of each tissue (use an initial guess for the first iteration).
- (8) Simulate the tissue deformation using FE analysis.
- (9) Extract stress distribution from the simulation and form vector $\{\sigma\}$ in equations (9) and (10).
- (10) Feed the results of steps 4 and 9 into equations (9) or (10) and calculate the updated hyperelastic parameter vector $\{C\}$ for each element and then average over each tissue volume.
- (11) Go to step 7 and set the hyperelastic parameters to the updated values ($\{C\}$) and repeat until the variations in the updated parameters are smaller than a tolerance value.

3.2. Hybrid regularization technique

The proposed reconstruction technique uses the pre- and post-deformation images of the tissue to measure the tissue displacements and uses these measurements to reconstruct the hyperelastic parameters (C_{ij} or C parameters in equations (9) and (10)). These displacements can be measured indirectly from the images corresponding to the tissue pre- and post-deformation or directly using MRI or US displacement data acquisition techniques. Using a least-squares method to solve the inverse problem formulated in equation (9), we obtain the following equation to calculate the parameters in each iteration:

$$C = (A^T A)^{-1} A^T \sigma. \quad (11)$$

Equation (11) requires calculating the inverse of the matrix $(A^T A)$, which is not always possible. For the Yeoh model, $(A^T A)^{-1}$ is a 3×3 matrix, which can be inverted easily. For the polynomial model, however, five parameters are involved, and it was observed that the inverse problem was highly ill posed; hence, the inversion was not possible without regularization. Equation (12) presents the SVD (singular value decomposition) representation of equation (9) and will be used in our regularization technique. For the Veronda–Westmann model the nonlinear system of equation (10) was solved using optimization techniques.

To invert the $(A^T A)$ matrix in the polynomial model case, a novel systematic hybrid regularization technique was developed. This technique is consisted of a sequence of three

known regularization techniques. Each of these techniques leads to a certain amount of error in the reconstructed parameters. The sequence of these techniques was selected based on the fact that the regularization methods known to lead to large errors (i.e. truncated SVD) are more stable during the initial iterations where errors are expected to be large, whereas methods known to be associated with high accuracy are usually unstable during the initial iterations (i.e. Weiner filtering). Therefore, the iterations were split into three intervals where each interval involves using a certain regularization technique.

The proposed sequence of the regularized iterative solution is designed such that each regularization technique is fully exploited according to its known accuracy and stability characteristics. In the first interval where the iterations begin, inversion accuracy is not very important; hence, the truncated SVD method given in equations (13) was used. If a proper number of eigenvalues are selected, this method is very stable while is not capable of finding the exact solution (i.e. leads to large error in reconstructed parameters). We found that using the first four eigenvalues ($q = 4$) while eliminating the last (smallest) eigenvalue led to a stable solution. This set of iterations is continued until the changes in the values of the reconstructed parameters were less than the specified threshold. The thresholds were selected by comparing the mean-squared difference between the stress-strain curves corresponding to two consecutive iterations and the value of 10^{-12} was selected as the threshold for the mean-squared distance:

$$\begin{aligned} \sigma &= AC, & q &= \text{rank}(A^T A) = 5, & e_i &: \text{eigenvalue} \\ A^T A &= USV^T, & U &= [u_1, \dots, u_q], & V &= [v_1, \dots, v_q]^T, & S &= \text{diag}(e_1, \dots, e_q) \end{aligned} \quad (12)$$

$$\hat{C} = \sum_{i=1}^{q'} \frac{u_i^T \sigma}{e_i} v_i, \quad q' = 4 < \text{rank}(A^T A). \quad (13)$$

Following this set of iterations in the first interval, we switched to the Tikhonov regularization technique with $\Gamma = \alpha I$ (equation (14)), where I is the identity matrix. Tikhonov regularization is capable of providing better solutions than the truncated SVD if the scaling parameter α is selected properly. There is a tradeoff between the stability and accuracy of the method, i.e. small scaling parameter (α) values result in smaller errors in the solution while contributing less to the system's stability and vice versa. Systematic methods of finding the optimal α values such as the L-curve technique can be used. We found the values of $\alpha = 10^{-4}$ and $\alpha = 10^{-2}$ to be suitable for the simulation and experimental studies, respectively. Again, this set of iterations is continued until the error either stops decreasing or reaches a steady state:

$$\hat{C} = (A^T A + \Gamma^T \Gamma)^{-1} A^T \sigma, \quad \Gamma = \alpha I. \quad (14)$$

Although the output of Tikhonov regularization is close to the exact values (if the scaling parameter is small enough), its accuracy still had room for improvement. As such, the Wiener filtering regularization technique (equation (15)) was used to achieve more accurate results in the final iteration interval:

$$\hat{C} = \sum_{i=1}^q f_i \frac{u_i^T \sigma}{e_i} v_i, \quad f = \left[1, 1, 1, 1, \frac{e_5^2}{e_5^2 + \alpha^2} \right]. \quad (15)$$

The Wiener filter is similar to Tikhonov regularization, but instead of modifying all the eigenvalues of the system, it enables modifying only a few of the eigenvalues while keeping the other ones unchanged. Here, we only changed the smallest one using the same values for the parameter α as the values used in Tikhonov regularization steps ($\alpha = 10^{-4}$ for

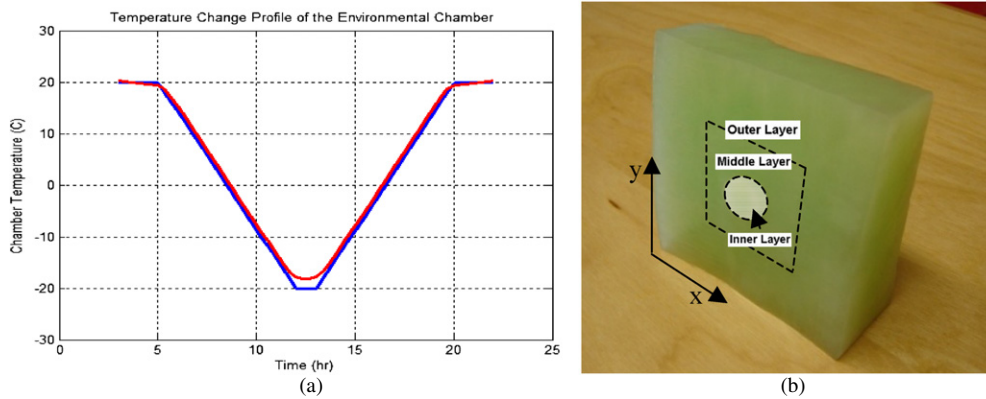


Figure 2. (a) Temperature change profile of the environmental chamber for one FTC which takes approximately 14 h. (b) The PVA phantom, consisting of three different tissue types. Two outer and middle cubic portions represent the adipose and fibroglandular tissues of the breast, while the inner cylindrical part represents a tumor.

simulation and $\alpha = 10^{-2}$ for experiment). Thus, the main system of equations does not change significantly as a result of this regularization leading to high accuracy. We found that this sequential regularization technique led to stable and reasonably accurate hyperelastic parameter reconstruction.

3.3. Polyvinyl alcohol (PVA) phantom construction

PVA is a material widely used for constructing tissue-mimicking phantoms with hyperelastic characteristics. To make the phantom, PVA was first dissolved in deionized water. The stiffness of PVA and its nonlinear characteristics depend on two factors: the PVA concentration and the number of freeze-thaw cycles (FTCs) the PVA goes through. During a FTC the PVA gel is frozen and then thawed systematically so that the PVA crystals form. An environmental chamber (Cincinnati Sub-Zero model ZH-8-1-H/AC) was used to perform this process. The chamber's temperature decreases gradually starting from the room temperature and drops down to -20°C . This decrease in the temperature takes place gradually and with a constant rate during 14 h. The temperature profile changed as shown in figure 2(a).

The larger the number of FTCs the stiffer the samples. In the case of a large phantom, different portions of the phantom undergo freeze and thaw cycles with different rates; therefore, it is difficult to make a PVA phantom with uniform properties. However this effect is reduced by changing the chamber temperature slowly over a long period of time (14 h).

The constructed phantom had the following characteristics. The inclusion, which is the stiffest part, was 10% PVA and five FTCs. The middle block of the phantom was made up of 5% PVA and three FTCs and the outer block was constructed using 5% PVA and two FTCs. This phantom is shown in figure 2(b). The phantom was constructed in three steps, starting from the inner cylindrical inclusion (1 cm diameter, 2 cm height), which underwent two FTCs. The middle cubic part was constructed by placing the inclusion in the middle of a mold built for the middle layer followed by pouring the 5% PVA surrounding the inclusion followed by 1 FTC. Finally the outer layer was built by placing the middle layer containing the inclusion inside a mould constructed for the outer layer and pouring 5% PVC followed by other two FTCs. This process was required to make the phantom while having bonding

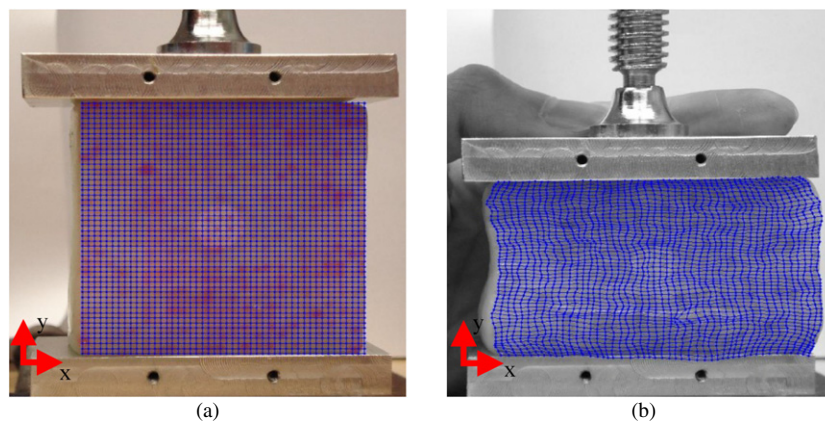


Figure 3. (a) Computational mesh overlaid over the mesh placed manually on the phantom's surface for displacement data acquisition prior to compression and (b) the meshes after compression.

between the three tissue layers. The mechanical properties of each PVA layer were measured independently using the cylindrical sample of the same material that underwent the same FTCs. These measurements are required to assess the amount of error in the reconstruction results. The uniaxial tests were performed using an electromechanical device developed in our laboratory (Samani and Plewes 2004). Having displacement resolution (step size) of $0.5 \mu\text{m}$ and load measurement accuracy of 0.0001N , this device is capable of recording the force and the amount of compression applied to the cylinder with high accuracy. The PVA samples had an equal height and diameter of approximately 10 mm. We acquired the force-deformation data for each sample after applying 1 g preload followed by compression of up to 2.5 mm. The hyperelastic parameters of each PVA layer sample were calculated using the force-deformation data in conjunction with equation (8).

3.4. Displacement tracking

The phantom was constructed in a way that it was close to plane stress situation. Its dimensions are $61 \text{ mm} \times 63 \text{ mm} \times 20 \text{ mm}$. A numerical experiment involving the phantom's 3D (accurate) and 2D (plane stress) FE models confirmed that with this thickness of 20 mm the plane stress assumption is valid. This experiment indicated maximum displacement errors of 2.68% and 5.3% in the plane's x -axis and y -axis, respectively. Using this assumption, only the displacements of the nodes on the surface were needed; hence, displacement data acquisition could be performed by tracking the phantom's surface deformation.

The iterative reconstruction process requires measuring the displacement of each point in the phantom as it undergoes compression stimulation. For this purpose, we used a simple inexpensive displacement-tracking method, which involves placing a 2D mesh on the phantom's surface and tracking the nodal displacements by manually processing the photos of the undeformed and deformed phantoms as shown in figure 3.

A 25×24 grid was created on the phantom's surface manually in a way that its nodes formed four-noded rectangular elements on the phantom. This grid was created by placing dots on the designed grid nodal points using a non-washable fine marker. Then, a photo of the phantom was acquired using a digital camera. The phantom was compressed by 31.6% while the bottom boundary was fixed using the compression set-up shown in figure 3. At

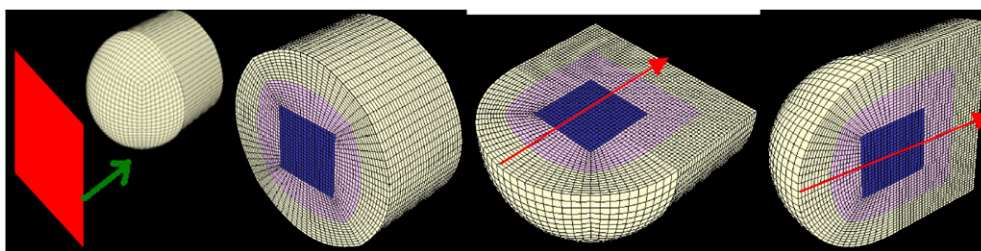


Figure 4. FE mesh of the computational breast phantom and three corresponding orthogonal cross sections. Different tissue types are shown in different colors, where the interior, middle and exterior layers represent tumor, fibroglandular and adipose tissues, respectively. The red arrow shows the direction of the applied compression.

this compressed state a new photo was taken using the same digital camera and from the same position. The photos of the phantom before and after compression and their meshes are depicted in figure 3. These meshes were used to model the phantom in the ABAQUS finite element solver. Using the acquired photos, we extracted the coordinates of each node manually from the pre-compression image and its corresponding node in the post-compression image using MATLAB's `imtool` command. To improve data acquisition accuracy, this manual node coordinate extraction was conducted by ten individuals, each of whom repeated the extraction three times. The acquired node coordinates were averaged and the two pre- and post-compression node coordinate sets were subtracted from each other to determine the displacements.

3.5. Method validation

To test the accuracy and robustness of the method for hyperelastic parameter reconstruction of breast tissues, we performed studies that involved numerical and tissue-mimicking breast phantoms.

3.5.1. Numerical phantom study. A numerical phantom study was performed on a simplified breast tissue geometry consisted of a hemisphere connected to a short cylinder. The breast phantom was composed of three tissue types to represent the two normal tissue types of fat and fibroglandular tissues in addition to a tumor tissue as shown in figure 4. In this numerical phantom, we assumed that the hyperelastic parameters of the normal breast tissues (the adipose and the fibroglandular tissues) are known, and we sought to determine the tumor's parameters. Samani and Plewes (2004) indicated that the hyperelastic parameters of the normal breast tissues can be measured independently. They reported these parameters for a polynomial model of normal breast tissues. Figure 5 shows the stress–strain relationship for the fat, fibroglandular and tumor tissues used in the numerical analysis to construct the model. The phantom's FE mesh was constructed using a transfinite interpolation meshing technique (TFI). The general TFI technique described in Rvachev *et al* (2000) uses four-noded and eight-noded elements to mesh 2D and 3D objects, respectively. It involves using blending functions to map a logical space of a unit square grid to a FE mesh of the given 2D shape bounded by four curves: left, right, upper and lower. This basic technique does not lead to a good quality FE mesh if the four boundaries are close to circle arcs. To address this weakness we used the TFI-based method described in Horgan and Gilchrist (2004). This method constructs a circular mesh by applying the TFI method to five meshes of quadrilateral

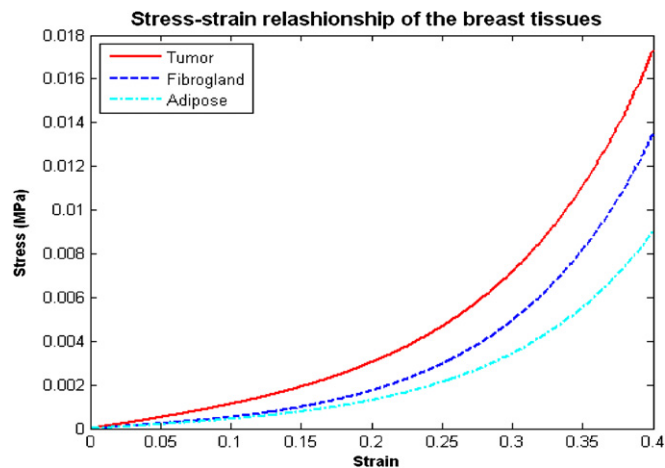


Figure 5. True stress–strain relationships of the fat, fibroglandular and tumor tissues used in the numerical model.

regions connected to each other. The advantage of using this method over the one using the basic TFI method is that the latter results in extremely distorted elements in regions close to the circle perimeter, while the former avoids having such elements leading to well-shaped elements (Mehrabian and Samani 2008). In our numerical study we used elements of type C3D8RH in ABAQUS which are eight-noded linear brick elements that use reduced integration with hourglass control. This type of elements uses hybrid with constant pressure formulation to account for tissue incompressibility. The mesh generated for the computational phantom with element corresponding to three tissue types is shown in figure 4.

Using prescribed displacement boundary conditions, the loading was applied to the top surface of the phantom along the axis of the cylindrical part as shown with the red arrows in figure 4. A moving rigid plate was used to compress the phantom while the displacement is being applied. The bottom surface of the phantom (bottom of the cylindrical part) was fixed (prescribed boundary condition) in the direction of loading. With the FE mesh used in our simulation, mesh locking and other convergence issues were minor at a 30% compression level and were overcome by reducing the ABAQUS analysis increment parameter size. 30% compression was applied to the numerical phantom using the nonlinear FE model we developed in ABAQUS. The analysis was performed for the three strain energy functions: the Yeoh, the polynomial and the Veronda–Westmann strain energy functions. The displacement field obtained from each FE analysis was fed to the reconstruction algorithm to obtain the tissues' hyperelastic properties. The input displacement field contains only small errors pertaining to the computer round-off process. The inverse problem was solved using the iterative algorithm summarized in figure 1. For the polynomial form we used the developed hybrid regularization technique to achieve convergence while the Yeoh and Veronda–Westmann models converged without any regularization.

3.5.2. Tissue-mimicking phantom study. The PVA phantom shown in figure 2(b) underwent 31.7% compression; this high amount of compression is required here since we are seeking

to determine the hyperelastic properties of the tissues, especially the tumor tissue as it is stiffer and consequently does not deform sufficiently with low compression. The phantom's baseline photo and a photo corresponding to its deformed state are depicted in figure 3. Uniaxial compression tests were performed on the cylindrical samples of each tissue type, and their hyperelastic properties were measured independently to validate the reconstruction results. Unlike the numerical phantom study where only one set of the tumor's parameters was assumed to be unknown, in this phantom study two ratio sets of the parameters of the tumor tissue to the parameters of the other normal tissues (fibroglandular and adipose tissue) were assumed to be unknown. Note that since the present approach employs the phantom's displacement data while no force information is available for data inversion, the algorithm is only capable of reconstructing the relative values of the parameters uniquely. Similar to classical elastography where linear elasticity is used leading to elastic modulus reconstruction, the relative hyperelastic parameter reconstruction proposed here can still be useful for cancer diagnosis as the reconstructed ratios can provide clues about how different is the suspicious mass from normal tissues.

4. Results

This section presents the results obtained from using our proposed reconstruction algorithm in the computational and tissue-mimicking breast phantom studies.

4.1. Reconstruction results

Table 1 presents the results of the numerical phantom study. This table shows the initial guess, true parameter values, reconstructed parameter values, number of iterations required for convergence, the tolerance used in the convergence criteria, and the percentage error of the calculated values for Yeoh, Veronda–Westmann and polynomial models, respectively. Reconstructed parameter tolerances were selected such that the mean-squared error (MSE) between stress–strain curves obtained from two consecutive iterations is less than 10^{-12} . Other values can be used to achieve other levels of accuracy.

The MSE between the stress–strain relationships corresponding to the reconstructed parameters versus that of the actual parameters in logarithmic scale at each iteration for the Yeoh, Veronda–Westmann and polynomial models are shown in figures 6(a)–(c), respectively. The logarithmic scale magnifies the errors leading to less-clear convergence in (a) and (b), which is otherwise very clear in the corresponding non-logarithmic scale figures (not shown).

In conjunction with the polynomial model, regularization was employed as the inverse problem proved to be highly ill posed. In this regularization technique, as described in section 3.2, we divided the iteration range into three regions as shown in figure 6(c). The dashed lines correspond to the first region where the truncated SVD method was used. The solid line portion of the graph corresponds to the second region where the Tikhonov regularization technique was used while the last portion (dash-dotted line) of the graph corresponds to the Wiener filtering regularization technique used for the third iteration region. The last portion shows a slight initial increase in the error which reached a plateau after the 70th iteration.

For the tissue-mimicking phantom, the iterative reconstruction approach was employed to reconstruct the ratios of the hyperelastic parameters as described earlier. Figures 7(a)–(c) show the MSE between the stress–strain relationships corresponding to the reconstructed parameters and parameters obtained from the uniaxial compression tests calculated at each iteration for the Yeoh, Veronda–Westmann and polynomial models, respectively.

Table 1. The initial guess, true values and reconstructed values of the hyperelastic parameters, number of iterations required to reach these values, the tolerances used as convergence criteria and the error percentage of the calculated hyperelastic parameters for the Yeoh, Veronda–Westmann and polynomial models.

	Initial guess (kPa)	True value (kPa)	Calculated value (kPa)	Iteration number	Tolerance (%)	Error (%)
C ₁₀ (Yeoh)	0.005	0.001 61	0.001 612	25	0.2	0.1
C ₂₀ (Yeoh)	0.03	0.0125	0.012 49	25	0.2	0.1
C ₃₀ (Yeoh)	0.01	0.00551	0.005 541	25	0.2	0.6
C ₁₀ (V-W)	0.01	0.0014	0.001 39	15	0.1	0.7
C ₂₀ (V-W)	0.01	−0.0048	−0.004 79	15	0.1	0.2
C ₃₀ (V-W)	20	5.0194	5.02	15	0.1	0.0
C ₁₀ (polynomial)	0.01	0.000 85	0.000 849	70	0.04	0.0
C ₀₁ (polynomial)	0.01	0.0008	0.000 799	70	0.04	0.0
C ₂₀ (polynomial)	0.01	0.004	0.004 065	70	0.04	1.6
C ₁₁ (polynomial)	0.01	0.006	0.005 883	70	0.04	1.9
C ₀₂ (polynomial)	0.01	0.008	0.008 051	70	0.04	0.7

These graphs confirm the convergence of the method to the final hyperelastic parameter values. It can be seen that the Yeoh model shows a very smooth convergence throughout the process. The Veronda–Westmann model shows more fluctuation as it approaches the convergence state due to the need for solving a nonlinear system of equation in this case. The polynomial model shows more instability despite that its inverse problem leads to a linear system in terms of the parameters. This instability is attributed to the system's high ill-conditioning, which necessitated employing the sequential regularization technique. With the polynomial model the truncated SVD regularization technique was used in the first 13 iterations after which the error became relatively steady. At this point the Tikhonov regularization technique was initiated. This was continued until the 46th iteration after which significant reduction in the error was not observed. Hence, Wiener filtering was initiated to refine the parameter accuracy.

Given that the hyperelastic parameters of breast adipose and fibroglandular tissues have limited intersubject variations, results obtained from this study are reported in the form of ratios of the inclusion's parameters to those of the middle and outer layer tissues. Table 2 provides the ratios of the C₁₀'s, C₀₁'s, C₂₀'s, C₁₁'s and C₀₂'s of the inclusion tissue to the middle layer tissue for the polynomial, Yeoh and Veronda–Westmann models. These ratios show an average parameter reconstruction error of 13%. Similarly, table 3 provides these ratios relative to the outer layer tissue, which shows an average reconstruction error of 9.6%.

5. Discussion and conclusions

The goal of this work was to develop a noninvasive technique to reconstruct breast tissue hyperelastic parameters that can potentially be used for *in vivo* measurement of these parameters for breast tissues. This was mainly motivated by the *ex vivo* breast tissue measurement findings that some hyperelastic parameters such as C₂₀ of the Yeoh model and C₁₁ and C₀₂ of the polynomial model can be used effectively for cancer detection and diagnosis (O'Hagan and Samani 2009). To achieve this goal, we used elastography and

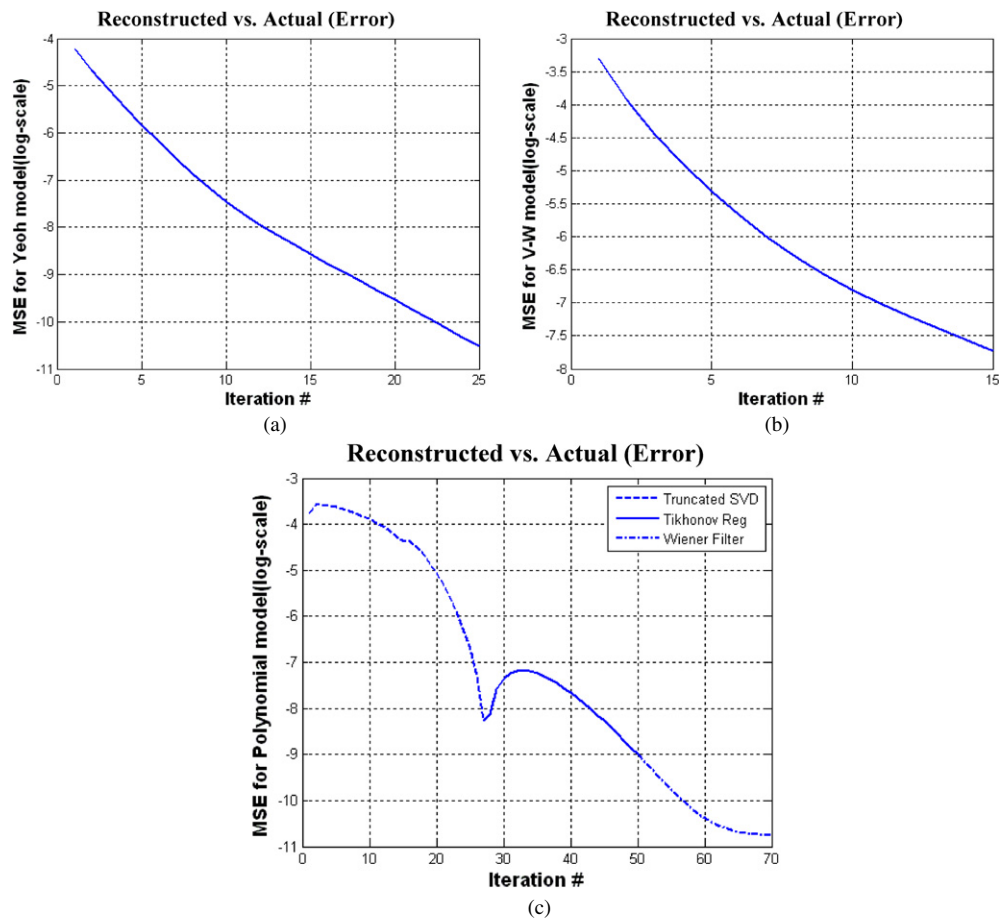


Figure 6. MSE (logarithmic scale) between the stress–strain relationships corresponding to the reconstructed parameters versus that of the actual parameters versus the number of iterations for the (a) Yeoh model, (b) Veronda–Westmann model and (c) polynomial model. In (c) the dashed line corresponds to the truncated SVD regularization technique, while the solid line and the dash-dotted line correspond to the Tikhonov and the Wiener filtering regularization techniques, respectively.

attempted to reconstruct hyperelastic parameters, which characterize the tissue nonlinear behavior. Given breast tissue nonlinearity, we used hyperelastic models to characterize their mechanical behavior as they are valid for a wide strain range expected in elastography imaging procedures. As such, another advantage of the proposed technique is that, unlike conventional breast elastography techniques, its reconstructed parameters can be interpreted irrespective of the amount of pre-compression applied to the breast prior to its mechanical stimulation in elastography procedures. This can facilitate reliable interpretation of elastography images.

In this investigation, we used three hyperelastic models that are used extensively in modeling soft tissues. These models are the second-order polynomial model with five parameters, the Yeoh model that has three parameters and the Veronda–Westmann model with three parameters. The hyperelastic parameter reconstruction was performed using the presented iterative approach. The problem was formulated as an inverse problem in which the parameters were updated at each iteration until convergence was achieved.

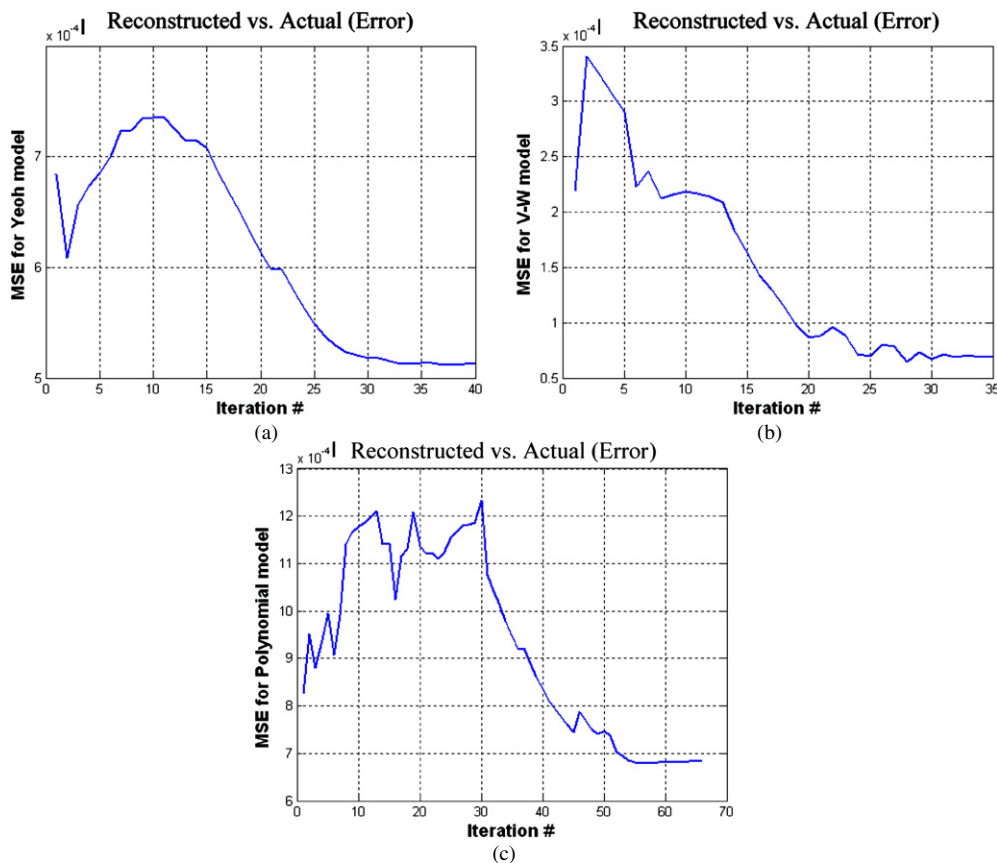


Figure 7. Error between the stress–strain relationships of the reconstructed and uniaxial test parameters versus the number of iterations for the (a) Yeoh model, (b) Veronda–Westmann model and (c) polynomial model.

To validate the proposed technique, numerical and tissue-mimicking phantom studies were performed. The goal of the numerical phantom study was to measure the hyperelastic parameters of the tumor tissue. The reconstruction obtained from this study showed excellent results, which encouraged us to proceed with the tissue-mimicking phantom study. As reported in table 1 all parameters were reconstructed with errors of less than 2%. In this numerical phantom study, it was noted that the inverse problem system of equations became ill conditioned for the polynomial model. To address this issue, we observed that solving the problem without regularization or even using traditional regularization techniques did not lead to acceptable solutions. Therefore, we developed a novel regularization technique that uses three different regularizing methods sequentially during the iterative reconstruction process. The proposed sequential regularized solution is designed such that each one of the regularization techniques is fully exploited according to its known accuracy and stability characteristics.

The impact of using this regularization technique is converging to an accurate and stable solution at the cost of relatively large number of iterations. For the Yeoh model, all three parameters were reconstructed with errors of less than 1% in a small number of iterations compared to the polynomial model (less than half the number of iterations). The polynomial

Table 2. Ratio of the C_{10} 's, C_{01} 's, C_{20} 's, C_{11} 's and C_{02} 's of the inclusion tissue to the middle layer tissue for both reconstruction and uniaxial test results and their error for the polynomial, Veronda–Westmann and Yeoh models.

	Reconstructed	Uniaxial test	Error (%)
C_{10_t}/C_{10_n2} (polynomial)	2.7	3.0	8.6
C_{01_t}/C_{01_n2} (polynomial)	2.1	2.0	4.7
C_{20_t}/C_{20_n2} (polynomial)	2.5	2.9	14.9
C_{11_t}/C_{11_n2} (polynomial)	2.5	2.8	9.5
C_{02_t}/C_{02_n2} (polynomial)	2.5	2.9	15.5
C_{10_t}/C_{10_n2} (Yeoh)	2.2	2.6	14.9
C_{20_t}/C_{20_n2} (Yeoh)	2.0	2.1	8.1
C_{30_t}/C_{30_n2} (Yeoh)	2.4	1.9	22.4
C_{10_t}/C_{10_n2} (V-W)	1.6	1.4	17.2
C_{20_t}/C_{20_n2} (V-W)	0.6	0.6	15.5
C_{30_t}/C_{30_n2} (V-W)	1.1	1.3	12.0

Table 3. Ratio of the C_{10} 's, C_{01} 's, C_{20} 's, C_{11} 's and C_{02} 's of the inclusion tissue to the outer layer tissue for both reconstruction and uniaxial test results and their error for the polynomial, Veronda–Westmann and Yeoh models.

	Reconstructed	Uniaxial test	Error (%)
C_{10_t}/C_{10_n1} (polynomial)	3.2	3.6	11.0
C_{01_t}/C_{01_n1} (polynomial)	3.5	3.8	7.8
C_{20_t}/C_{20_n1} (polynomial)	11.6	11.0	5.3
C_{11_t}/C_{11_n1} (polynomial)	11.5	10.7	7.5
C_{02_t}/C_{02_n1} (polynomial)	11.0	11.1	1.5
C_{10_t}/C_{10_n1} (Yeoh)	4.1	4.5	8.5
C_{20_t}/C_{20_n1} (Yeoh)	5.4	4.8	12.6
C_{30_t}/C_{30_n1} (Yeoh)	9.6	8.3	15.3
C_{10_t}/C_{10_n1} (V-W)	2.3	2.1	10.0
C_{20_t}/C_{20_n1} (V-W)	2.3	2.8	18.8
C_{30_t}/C_{30_n1} (V-W)	1.5	1.7	7.0

model depends on the strain invariants I_1 and I_2 , while the Yeoh model depends only on one strain invariant I_1 . Dependence on the second invariant makes the system unstable. The Yeoh model converges in fewer iterations than the polynomial model yet leading to higher accuracy; therefore, eliminating I_2 -dependent terms in the strain energy function results in higher stability in the system.

For the case of the Veronda–Westmann model, convergence was achieved in even smaller number of iterations than the Yeoh model resulting in errors smaller than 1%. This demonstrates the efficiency of the Veronda–Westmann model compared to the Yeoh model. Although the Veronda–Westmann model like the polynomial model is dependent on both I_1 and I_2 strain invariants whereas Yeoh model is only dependent on the I_1 strain invariant, its fast convergence can be attributed to the exponential form of the Veronda–Westmann model, which is intrinsically more suitable for biological tissue response. As shown in figure 6(b), the method converges in a smoother fashion and requires a few iterations compared to other

models. The difficulty encountered in this case was the need to solve nonlinear system of equations. Nonetheless, no convergence or solution uniqueness issues were encountered.

In the last study, we constructed a phantom using PVA that exhibits nonlinear mechanical behavior after undergoing FTCs. In this study, we used cylindrical samples of each tissue type to measure their hyperelastic properties independently using uniaxial tests. To acquire tissue displacements in this study, a mesh was placed on the surface of the phantom and the displacement data were extracted manually from the pre- and post-compression photos of the phantom. In this study the ratio of the hyperelastic parameters of the inclusion to those of the background tissues were reconstructed. As reported in tables 2 and 3, the relative reconstruction led to reasonably accurate results with average reconstructed parameter errors of 13% and 9.6%.

For the polynomial model, similar to the numerical study, we encountered an ill-conditioned system of equations. The same sequential regularization technique was used here to guide the algorithm toward convergence. Again, convergence required a large number of iterations and the reconstruction error was modest due to the combination of regularization and experiment errors. For the Yeoh model, although the number of iterations was less than that for the polynomial model, we observed larger errors in the reconstructed ratios compared to the polynomial model. This can be attributed to the fact that the Yeoh model is dependent on the first invariant (I_1) only. The Veronda–Westmann model converged in even fewer iterations; however, the error in the system is relatively higher than that of the polynomial model's counterpart but less than that of the Yeoh model.

Compared to the errors observed in the numerical phantom study, the errors encountered in the tissue-mimicking study are significantly larger. This can be mainly attributed to two factors. One is the error is associated with the manually measured tissue displacements used as input in the inverse problem algorithm. This error was mainly due to that the mesh nodes were marked on the phantom's surface using a fine point marker. Despite that the used marker was non-washable, the ink diffused over the surface leading to ill-defined nodes on the surface. Major improvement can be expected with using more accurate image-based displacement data acquisition techniques such as MRI phase imaging (Chenevert *et al* 1998).

The other source of error is related to the difference between the hyperelastic parameters of the tissue layers with their corresponding cylindrical samples. Although both were made from the same PVA concentration and underwent the same freeze-thaw temperature conditions, different geometries imply different spatial temperature distribution over time leading to different chemical bond forming process. The latter may lead to significant tissue stiffness evolution. Another difficulty of implementing this technique especially in clinical cases is the requirement for segmenting the breast tissue into its different tissue types. This requires detecting the presence of a suspicious region in the breast tissue and segmenting it prior to applying the reconstruction technique. Note that, as concluded by Samani *et al* (2001), the conventional image segmentation techniques such as thresholding are sufficient for this purpose since the reconstruction averaging step minimizes the impact of segmentation errors.

Overall, based on our experimental and simulation studies, the Veronda–Westmann model is the best model for breast tissue modeling among the three studied models. This is true for two reasons: one is that its accuracy is higher than the Yeoh model and the other is that its system of equations associated with inversion is more stable than that of the polynomial model. Moreover, the accuracy achieved in this phantom study is reasonably good considering the issues encountered in the experiments. The major issue of the input errors resulting from the manual displacement data acquisition is not significant in the clinic where MRI imaging can be utilized for displacement data acquisition. Even with the achieved accuracy, the proposed method seems to have good potential for breast cancer detection and diagnosis.

References

- Barbone P E and Oberai A A 2007 Elastic modulus imaging: some exact solutions of the compressible elastography inverse problem *Phys. Med. Biol.* **52** 1577–93
- Cespedes I, Ophir J, Ponnekanti H and Maklad N 1993 Elastography: elasticity imaging using ultrasound with application to muscle and breast *in vivo* *Ultrason. Imaging* **15** 73–88
- Chenevert T L, Skovoroda A R, O'Donnell M and Emelianov S Y 1998 Elasticity reconstructive imaging by means of stimulated echo MRI *Magn. Reson. Med.* **39** 482–90
- Devi C U, Chandran R S B, Vasu R M and Sood A K 2006 Elastic property estimation using ultrasound assisted optical elastography through remote palpation—a simulation study *Proc. SPIE* **6164** 61640Q
- Doyley M M, Meaney P M and Bamber J C 2000 Evaluation of an iterative reconstruction method for quantitative elastography *Phys. Med. Biol.* **45** 1521–40
- Emelianov S Y, Skovoroda A R, Lubinski M A and O'Donnell M 1995 Reconstructive elasticity imaging *Acoustical Imaging* vol 21, ed J P Jones (New York: Plenum Press) pp 241–52
- Erkamp R Q, Emelianov S Y, Skovoroda A R and O'Donnell M 2004 Nonlinear elasticity imaging: theory and phantom study *IEEE Trans. Ultrason. Ferroelectr. Freq. Control* **51** 532–9
- Gao L, Parker K J, Lerner R M and Levinson S F 1996 Imaging of the elastic properties of tissue—a review *Ultrasound Med. Biol.* **22** 959–77
- Hall T J, Oberai A A, Barbone P E, Sommer A M, Gokhale N H, Goenezen S and Jiang J 2009 Elastic nonlinearity imaging *31st Annual Int. Conf. IEEE EMBS* article no. 5333442, pp 1967–70
- Holzappel G A 2000 *Nonlinear Solid Mechanics: A Continuum Approach for Engineering* (Chichester: Wiley)
- Holzappel G A and Ogden R W 2003 *Biomechanics of Soft Tissue in Cardiovascular Systems* (New York: Springer Wien)
- Horgan T J and Gilchrist M D 2004 Influence of FE model variability in predicting brain motion and intracranial pressure changes in head impact simulations *Int. J. Crashworthiness* **9** 401–18
- Kaliske M and Rothert H 1997 On the finite element implementation of rubber-like materials at finite strains *Eng. Comput. (Swansea, Wales)* **14** 216–32
- Kallel F and Bertrand M 1996 Tissue elasticity reconstruction using linear perturbation method *IEEE Trans. Med. Imaging* **15** 299–313
- Konofagou E and Ophir J 1998 A new elastographic method for estimation and imaging of lateral displacements, lateral strains, corrected axial strains and Poisson's ratios in tissues *Ultrasound Med. Biol.* **24** 1183–99
- Manduca A, Oliphant T E, Dresner M A, Mahowald J L, Kruse S A, Amromin E, Felmlee J P, Greenleaf J F and Ehman R L 2001 Magnetic resonance elastography: non-invasive mapping of tissue elasticity *Med. Image Anal.* **5** 237–54
- Mehrabian H and Samani A 2008 An iterative hyperelastic parameters reconstruction for breast cancer assessment *Proc. SPIE* **6916** 69161C
- Mehrabian H and Samani A 2009 Constrained hyperelastic parameters reconstruction of PVA (Polyvinyl Alcohol) phantom undergoing large deformation *Proc. SPIE* **7261** 72612G
- Oberai A A, Gokhale N H, Goenezen S, Barbone P E, Hall T J, Sommer A M and Jiang J 2009 Linear and nonlinear elasticity imaging of soft tissue *in vivo*: demonstration of feasibility *Phys. Med. Biol.* **54** 1191–207
- O'Hagan J J and Samani A 2009 Measurement of the hyperelastic properties of 44 pathological *ex vivo* breast tissue samples *Phys. Med. Biol.* **54** 2557–69
- Ophir J, Cespedes I, Ponnekanti H, Yazdi Y and Li X 1991 Elastography: a quantitative method for imaging the elasticity of biological tissues *Ultrason. Imaging* **13** 111–34
- Plewes D B, Bishop J, Samani A and Sciarretta J 2000 Visualization and quantification of breast cancer biomechanical properties with magnetic resonance elastography *Phys. Med. Biol.* **45** 1591–610
- Rvachev V L, Sheiko T I, Shapiro V and Tsukanov I 2000 Transfinite interpolation over implicitly defined sets *Technical Report SAL*
- Samani A, Bishop J and Plewes D B 2001 A constrained modulus reconstruction technique for breast cancer assessment *IEEE Trans. Med. Imaging* **20** 877–85
- Samani A and Plewes D 2004 A method to measure the hyperelastic parameters of *ex vivo* breast tissue samples *Phys. Med. Biol.* **49** 4395–405
- Samani A and Plewes D 2007 An inverse problem solution for measuring the elastic modulus of intact *ex vivo* breast tissue tumours *Phys. Med. Biol.* **52** 1247–60
- Samani A, Sack I and Plewes D B 2003 Constrained nonlinear elasticity reconstruction technique for breast MRI elastography *Proc. ISMRM 11th Ann. Meeting* p 773
- Samani A, Zubovits J and Plewes D 2007 Elastic moduli of normal and pathological human breast tissues: an inversion-technique-based investigation of 169 samples *Phys. Med. Biol.* **52** 1565–76

- Sciarretta J, Samani A, Bishop J and Plewes D B 2002 MR validation of soft tissue mimicking phantom deformation as modeled by nonlinear finite element analysis *Med. Phys.* **29** 65–72
- Sinkus R, Weiss S, Wigger E, Lorenzen J, Dargatz M and Kuhl C 2002 Nonlinear elastic tissue properties of the breast measured by MR-elastography: initial *in vitro* and *in vivo* results *Proc. ISMRM 10th Ann. Meeting* p 33
- Skovoroda A R, Emelianov S Y, Lubinski M A, Sarvazyan A P and O'Donnell M 1994 Theoretical analysis and verification of ultrasound displacement and strain imaging *IEEE Trans. Ultrason. Ferroelectr. Freq. Control* **41** 302–13
- Skovoroda A R, Emelianov S Y and O'Donnell M 1995 Tissue elasticity reconstruction based on ultrasonic displacement and strain images *IEEE Trans. Ultrason. Ferroelectr. Freq. Control* **42** 747–65
- Skovoroda A R, Lubinski M A, Emelianov S Y and O'Donnell M 1999 Reconstructive elasticity imaging for large deformations *IEEE Trans. Ultrason. Ferroelectr. Freq. Control* **46** 523–35
- Sumi C, Suzuki A and Nakayama K 1995 Estimation of shear modulus distribution in soft tissue from strain distribution *IEEE Trans. Biomed. Eng.* **42** 193–202
- Varghese T, Ophir J and Krouskop T A 2000 Nonlinear stress–strain relationships in tissue and their effect on the contrast-to-noise ratio in elastograms *Ultrasound Med. Biol.* **26** 839–51
- World Health Organization 2006 *Fact sheet No. 297: Cancer* Retrieved on 26 April 2007
- World Health Organization International Agency for Research on Cancer 2003 *World Cancer Report* Retrieved on 02 March 2008
- Yamashita Y and Kawabata S 1995 Longitudinal compression property of wool fiber *Proc. 24th Text. Research Symp. (Mt. Fuji)* pp 16–21
- Zhang G 2004 Geometric and material nonlinearity in tensioned wires of an external fixator *Clin. Biomech.* **19** 513–8